Journal of Materials Chemistry A

PAPER

View Article Online
View Journal | View Issue

Cite this: J. Mater. Chem. A, 2019, 7, 14253

Topological semimetal porous carbon as a high-performance anode for Li-ion batteries†

Huanhuan Xie, [a] Yu Qie, [a] Muhammad Imran [a] and Qiang Sun *[abc]

Received 4th April 2019
Accepted 18th May 2019

DOI: 10.1039/c9ta03587g

rsc.li/materials-a

Motivated by the advantages of inherent high electronic conductivity and ordered porosity of topological semimetal monoclinic C_{16} (m-C_{16}), we explore its possible use as a lithium-ion battery anode material. Using state-of-the-art theoretical calculations, we show that the m-C_{16} structure has a high specific capacity of 558 mA h g^{-1}, a low Li ion diffusion energy barrier of 0.25 eV, and a small volume change of 3.6% during charging/discharging operation. The overall performance of m-C_{16} is superior to that of topological semimetal body-centered orthorhombic C_{16} (bco-C_{16}) reported recently with corresponding values of 558 mA h g^{-1}, 0.53 eV and 13.4%. This study further expands the family of porous topological carbon for high-performance anode materials going beyond the commercially used graphite.

1. Introduction

Batteries are collections of electrochemical cells, each composed of two electrodes that are separated by an electrolyte, which power the modern technological world.[1,2] Their applications vary from portable electronic devices to large scale power grid systems which require steady and sustainable power source supplies.[3,4] Compared to other kinds of batteries, the most widely used lithium-ion batteries (LIBs) have several advantages such as their compact size, high efficiency and good performance in a wide temperature range.[5–8] In the past two decades, computational methods have made great developments, and nowadays many major properties of LIBs can be accurately predicted by first principles calculations.[9,10] They have been widely used in lithium-ion battery electrode materials to explore the lithium-intercalation mechanism, and for diffusion energy barrier calculation, and structural stability and lithium insertion mechanism research.[11–13]

The development of LIBs has been hindered by safety and cost issues and limited by the low specific capacity problem.[14,15] Finding high performance electrode materials and optimizing the electrolyte for the system will be the key to deal with most of the challenging problems.[16–18] Graphite, which is a commercial anode for LIBs, has good stability and low cost. However, its theoretical maximum specific capacity is only 372 mA h g^{-1}, which cannot meet the higher requirements of current (capacity for electric vehicles) and future applications.[19] Si- and P-based materials are once considered as hopeful candidates because of their extremely high specific capacities (4200 and 2596 mA h g^{-1}, respectively). Nevertheless, they both suffer from poor reversibility caused by tremendous volume expansion and slow rate capability because of poor electronic conductivity.[20,21] To satisfy the rising demand for high-performance batteries with large-energy storage capacity, tremendous effort has been devoted to exploring new materials to enhance the specific energy and energy density of LIBs.[22,23] At the same time, the ability to quickly charge and discharge a battery, *i.e.*, the rate capability, is also a vital factor to make electric vehicles competitive.[24,25]

Considering the requirements of good reversibility, low cost and nontoxicity, carbon materials have some distinct superiorities as anodes.[26,27] In fact, besides graphite, graphene, carbon nanotubes (CNTs), carbon nanofibers (CNFs), and porous carbon have been widely studied for this purpose.[28–32] Porous carbon materials are of specific interest as their high specific surface area provides numerous binding sites for Li ions, which is beneficial for high-capacity LIB anodes.[33] Especially, recent research on topological semi-metallic porous carbon materials has given us some new insights into developing novel materials with good electrical conductivity going beyond the conventional ones.[34–36] These three dimensional (3D) topological carbon materials have intrinsic ordered nano-pores as well as high electrical conductivity, which can overcome the problem of low conductivity of traditional disordered porous carbon materials and thus provide new options for anode materials. This idea has been recently implemented in all-carbon-based porous topological semimetal bco-C_{16} that was proposed to be a promising LIB anode material[37] with a specific capacity of 558 mA h g^{-1}, corresponding to Li–C_4, which is 1.5 times larger than that of graphite (Li–C_6).

[a]Department of Materials Science and Engineering, College of Engineering, Peking University, Beijing 100871, China. E-mail: sunqiang@pku.edu.cn
[b]Center for Applied Physics and Technology, Peking University, Beijing 100871, China
[c]Key Lab of Theory and Technology for Advanced Batteries Materials, College of Engineering, Peking University, Beijing 100871, China

† Electronic supplementary information (ESI) available. See DOI: 10.1039/c9ta03587g

However, the main problem for topological semimetal bco-C_{16} is the significant volume expansion (13.4%) which is larger than the value of 10% in graphite.[37] Then a question arises: can we find a topological semimetal carbon allotrope with small volume expansion while keeping other good features? Here we show that the topological nodal-line m-C_{16} can fit this requirement.[34] By performing a detailed study on the Li intercalation and diffusion process in m-C_{16}, we demonstrate that Li atoms are able to intercalate into m-C_{16} with stable Li adsorption instead of phase separation. The maximum Li concentration is Li–C_4 (558 mA h g^{-1}), the same as that in bco-C_{16}. Lithium ions diffuse along a one-dimensional (1D) channel in m-C_{16}, with a much smaller energy barrier (0.25 eV) than that of bco-C_{16} (0.53 eV), resulting from the larger channel size of m-C_{16} than that of bct-C_{16}. In addition, the structure of sp^2–sp^3 hybridized m-C_{16} is more robust than that of all-sp^2 bonding bco-C_{16}. Thus the volume change during the Li charge and discharge process of m-C_{16} (3.6%) is smaller than that of bco-C_{16} (13.4%). Moreover, the 1D Li ion diffusion is robust against compressive and tensile strains. Based on the above findings, m-C_{16} is expected to be a promising anode material for LIBs.

2. Computational method

Since the pioneering work on using first-principles calculations for identifying cathode materials for batteries by Ceder *et al.*,[38] computation has been widely used for exploring new battery materials ranging from anodes to cathodes and electrolytes.[39–44] In this work, first-principles calculations are performed based on density-functional theory (DFT) by using the Vienna *Ab initio* Simulation Package (VASP) with the projector augmented wave (PAW) method.[45,46] A cutoff kinetic energy of 600 eV is chosen for the plane wave basis. For the exchange–correlation energy, we employ the Perdew–Burke–Ernzerhof (PBE) functional.[47] The effect of van der Waals (vdW) interaction is taken into account using the semiempirical generalized gradient approximation (GGA) type density functional constructed with a long-range dispersion correction by Grimme (DFT-D2 method).[48] Based on the test of convergence accuracy, we use (4 × 21 × 12) and (2 × 3 × 2) Monkhorst–Pack *k*-point meshes to represent the reciprocal space of the unit cell and supercell, respectively. By using the conjugated gradient algorithm, the crystal structure is fully optimized, the convergence criteria for energy and force are set to be 10^{-6} eV and 0.01 eV $Å^{-1}$, respectively. For the calculation of the lithium ion diffusion energy barrier and the minimum energy pathways, we use the method of climbing-image nudge elastic band (CI-NEB) as implemented in VASP transition state tools.[49,50]

3. Results and discussion

3.1 Single Li atom insertion and diffusion in m-C_{16}

The structure of m-C_{16} has a monoclinic primitive cell with a space group *C*2/*m* (no. 12) and contains 16 carbon atoms in each cell.[34] Its optimized lattice parameters are $a = 12.7988$ Å, $b = 2.4461$ Å, $c = 4.2766$ Å, and $\beta = 88.4°$. As shown by the band structure in Fig. S1 of the ESI,† m-C_{16} is a topological nodal-line semimetal with linear dispersion Dirac feature bands near the Fermi level, which is in agreement with the previous result.[34] Phonon spectrum calculations and first principles molecular dynamics (AIMD) simulations at 300 K are performed to verify the structural stability. The results are shown Fig. S2 in the ESI,† where no imaginary frequencies appear throughout the entire Brillouin zone, confirming that m-C_{16} is dynamically stable. Moreover, after heating for more than 5 ps, no obvious structural deformation occurred, and the total energy fluctuates around a constant without attenuation, suggesting that m-C_{16} is thermally stable at room temperature as well. Due to the special atomic configuration, m-C_{16} has a remarkable porous structure with a low density of 2.31 g cm^{-3}. The BET surface area of m-C_{16} is calculated to be 203 m^2 g^{-1}, which is relatively small compared to other porous carbon anode materials such as Hex-C_{18} (405 m^2 g^{-1}),[51] T-C_{24} (1286 m^2 g^{-1}),[36] and HZGM-42 (1316 m^2 g^{-1}).[6] Note that a small BET surface area would reduce the occurrence of side reactions between the electrolyte and the electrode, thus leading to a higher first cycle coulombic efficiency. So m-C_{16} would exhibit a merit in this aspect.

We then study the insertion of single Li atoms into m-C_{16}. To avoid the interaction of Li atoms, we use a 1 × 3 × 4 supercell. According to the symmetry of the structure, three possible

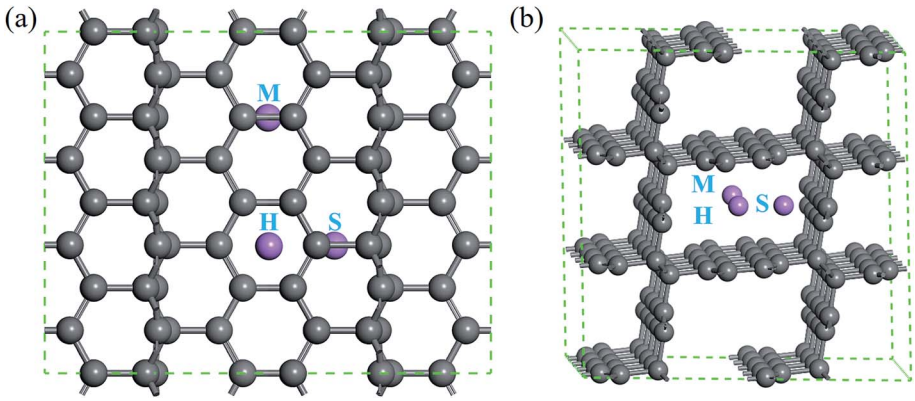

Fig. 1 Top (a) and side (b) views of the supercell structure of m-C_{16} and the schematics of the possible Li-ion absorption sites marked as M, H and S.

initial insertion sites are considered: the bridge site M (in the midpoint of the C–C bond), the hollow site H (in the center of the carbon hexagon), and the side site S (on one side close to the hole), as can be seen in Fig. 1. After the structure is optimized, we find that Li atoms move from the M and S sites to the adjacent H sites. This suggests that, at dilute concentration, H sites are the most stable adsorption positions for Li atoms. The Bader charge population analysis reveals that there is $0.89|e|$ charge transferred from Li atoms to the m-C_{16} substrate, indicating that Li atoms contribute most of their s electrons and then become Li ions. This leads to strong Coulomb repulsion between lithium ions and prevents them from clustering to form lithium dendrites. To visualize the effect of Li atom adsorption on the charge distribution of the m-C_{16} substrate, we calculated the bonding charge density which is the difference between the charge density before and after absorption. Fig. S3 of the ESI† illustrates the bonding charge density difference, where red and green colors indicate the electron accumulation and depletion respectively and one can see that the charge is transferred from the adatoms to the m-C_{16} substrate.

To further investigate the interaction between Li ions and the substrate, we calculate the Li ion binding energy (E_b), which can be defined as

$$E_b = \frac{E_{Li_x\text{-m-}C_{16}} - E_{\text{m-}C_{16}} - x\mu_{Li}}{x} \quad (1)$$

where $E_{Li_x\text{-m-}C_{16}}$ and $E_{\text{m-}C_{16}}$ are the total energies of the Li-inserted structure and original m-C_{16} crystal, respectively. μ_{Li} is the chemical potential of Li which is regarded as the atomic cohesive energy of metallic Li. The calculated E_b of Li ion

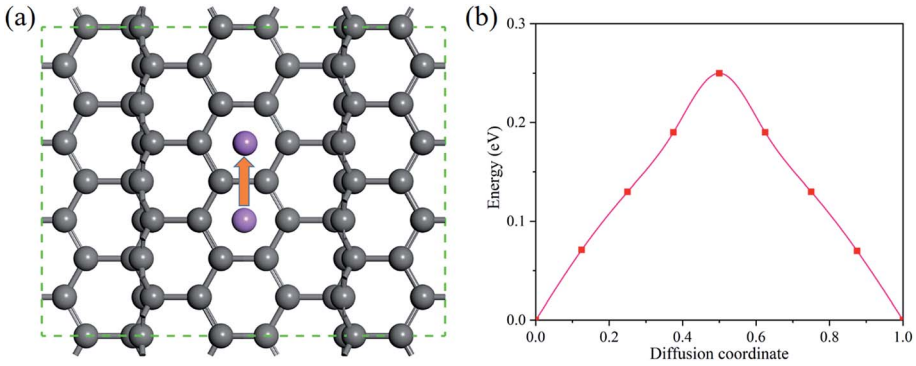

Fig. 2 (a) Schematics of the Li diffusion pathway along the one-dimensional diffusion channel. (b) The corresponding energy profile.

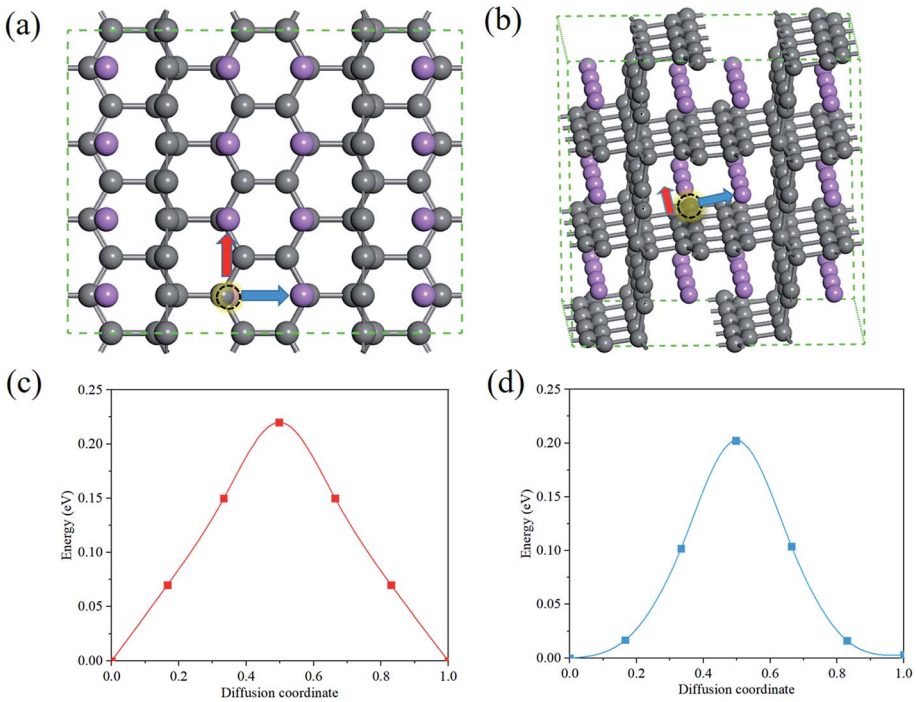

Fig. 3 (a) Top and (b) side views of the fully Li-intercalated configuration of m-C_{16}, and the two vacancy diffusion pathways marked by red and blue arrows. The corresponding energy profiles are presented in (c) and (d).

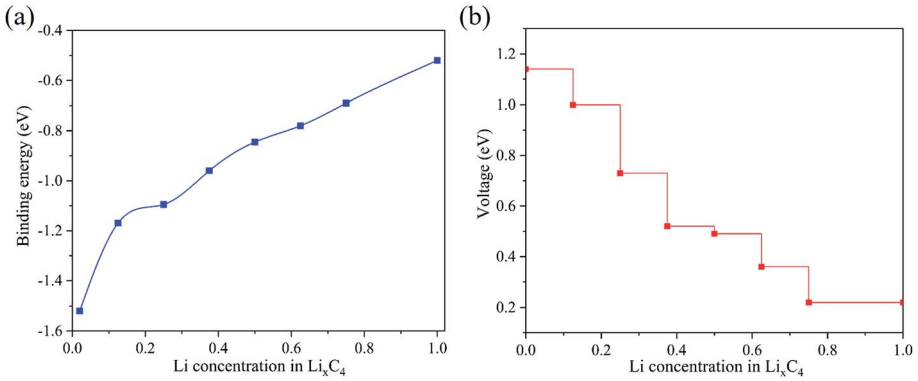

Fig. 4 (a) Binding energy profile and (b) voltage profile of six stable intermediate phases.

adsorption at the H position is −1.52 eV. The absolute value is much larger than that of graphite (−0.78 eV),[37,52] suggesting a strong ionic binding between Li ions and the m-C_{16} substrate.

We next calculate the energy barrier for Li ion diffusion. The Li-ion mobility determines the rate performance which plays an important part in the electrode material. Considering the symmetry of m-C_{16}, there is only one possible diffusive pathway: path along the 1D channel, as shown in Fig. 2(a). Based on climbing-image nudge elastic band (CI-NEB) calculations, the energy profile is presented in Fig. 2(b). There is only one energy peak with the corresponding energy barrier of 0.25 eV, which is comparable to that of graphite (0.218–0.400 eV),[53,54] indicating a high-rate capability of m-C_{16} for LIBs. On the basis of diffusion theory, the spatial dimension has an inverse effect on the diffusion constant, *i.e.* $D \propto \frac{1}{2}n$, where n is the dimension of space. Therefore, the lithium ions that migrate along the 1D channel are the fastest and have the highest migration efficiency.

3.2 Li storage capacity and theoretical voltage profile

To determine the maximum storage capacity, we study the fully Li-embedded m-C_{16} configuration, which is shown in Fig. 3. When Li atoms are fully intercalated in m-C_{16}, the position of the adsorption site has changed, and Li atoms trend to adsorbed in the S position. So four Li atoms could be adsorbed in one m-C_{16} unit cell, corresponding to Li–C_4. The maximum theoretical storage capacity of m-C_{16} is 558 mA h g^{-1}, which is 1.5 times the capacity of graphite (Li–C_6). The calculated binding energy E_b is −0.63 eV when all S positions are occupied by the Li ions; the binding is stronger than that of graphite (−0.11 eV) and $Ti_3C_2(OH)_2$ (−0.14 eV),[55] and is comparable to that of Ti_3C_2 (ref. 56) and Hex-C_{18} (−0.42 eV).[51] This indicates that Li ions can be stably adsorbed in m-C_{16} without causing phase separation problems at such a high Li concentration. We remove one Li ion from the fully Li-intercalated situation and calculate the vacancy energy barriers to estimate the diffusion properties of Li ions at high concentrations. Schematics of the vacancy diffusion pathways are shown in Fig. 3. There are two different pathways, and the calculated energy barriers are 0.22 and 0.20 eV, respectively. Compared to the migration of single Li ions, the energy barriers are slightly reduced.

To determine the electronic conductivity after Li atom adsorption in the m-C_{16} substrate, we calculate the total density of states (DOS) and partial DOS and the results are present in Fig. S4 of the ESI,† which suggest that the studied m-C_{16} anode would keep the metallic feature after Li atom adsorption. We can also see that there is an obvious overlap from −5 eV to the Fermi level between the C-2p orbital and the Li-2s orbital, indicating s–p orbital hybridization and strong interaction between Li atoms and the m-C_{16} substrate.

The voltage profile is important for measuring the performance of batteries.[11,57] The charge and discharge processes of m-C_{16} can be described with the following half-cell reaction:

$$(x_2 - x_1)Li^+ + (x_2 - x_1)e^- + Li_{x_1}\text{–m-}C_{16} \leftrightarrow Li_{x_2}\text{–m-}C_{16} \quad (2)$$

When neglecting the effects of volume, pressure, and entropy, the average voltage of Li_x–m-C_{16} within such a concentration range of $x_1 < x < x_2$ can be evaluated as

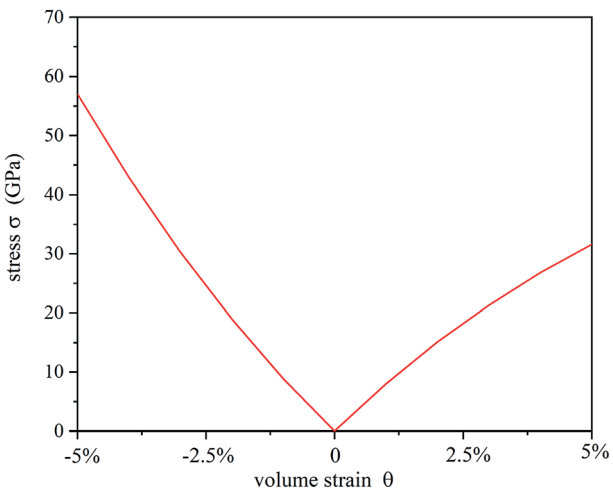

Fig. 5 Compressive and tensile stress σ as a function of volume strain θ.

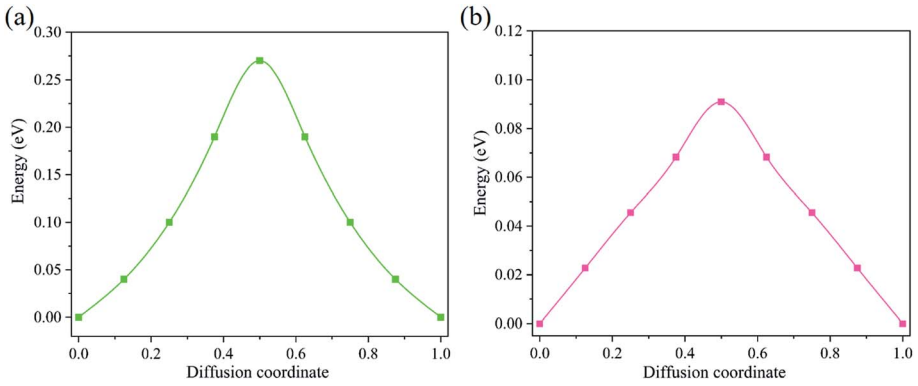

Fig. 6 Migration energy profiles under (a) 5% compressive strain and (b) 5% tensile strain.

$$V \approx \frac{E_{\mathrm{Li}_{x_1}\text{-m-C}_{16}} - E_{\mathrm{Li}_{x_2}\text{-m-C}_{16}} + (x_2 - x_1)E_{\mathrm{Li}}}{(x_2 - x_1)e} \quad (3)$$

where $E_{\mathrm{Li}_{x_1}\text{-m-C}_{16}}$, $E_{\mathrm{Li}_{x_2}\text{-m-C}_{16}}$ and E_{Li} are the total energy of Li_{x_1}-m-C_{16}, Li_{x_2}-m-C_{16}, and metallic Li, respectively.

In order to calculate the average voltage, we first look for the most stable Li ion occupied configurations at different intermediate concentrations. We select six intermediate concentrations (Li_xC_4: x = 0.125, 0.25, 0.375, 0.5, 0.625, 0.75). At each intermediate concentration, we examine the possible inequivalent adsorption configurations. By comparing the energy of different configurations, we identify the most stable configuration for each intermediate concentration, where the thermodynamic stability is verified through AIMD calculation, and the corresponding configurations and AIMD simulation results are presented in Fig. S5 and S6 of the ESI.†

At different Li ion adsorption concentrations, the binding energies are all negative. This indicates that Li ions can be stably adsorbed without forming clusters. In addition, the absolute value of the binding energy decreases as the concentration of lithium ions increases. This is mainly because the mutual repulsion between lithium ions is increased, while the interaction between lithium ions and the substrate weakened because of the reduced charge transfer from Li to m-C_{16} at high concentrations. Based on the obtained results, we calculate the average voltage using eqn (3). As seen in Fig. 4, at dilute concentrations (x < 0.375), the voltage has a uniform and relatively large drop from 1 V to 0.5 V; then, the voltage profile slowly drops to 0.22 V as the concentration of Li ions increases to 1. Moreover, the voltage maintains a positive value throughout the entire process, indicating that the half-cell reaction can be carried out spontaneously to reach the final phase (Li–C_4). The average voltage calculated by averaging of the voltage profile is 0.56 V, which is larger than those of graphite (0.11 V)[58] and bco-C_{16} (0.23 V),[37] but smaller than those of IGN (0.66 V),[42] MoC_2 (0.68 V),[59] 2D VS_2 (0.93 V)[58] and TiO_2 (1.5–1.8 V).[60]

3.3 Assessments of the cycling stability

Cycling stability is essential for practical application, which can be evaluated from the volume changes during the charging and discharging process. We compare the fully lithium occupied m-C_{16} with the original structure and find that no bond breaking arises and the total volume increase is only 3.6%, which is much lower than that of graphite (10%) and bct-C_{16} (13%). Comparing the lattice constants before and after the adsorption of lithium ions, we find that the volume expansion of the material is isotropic. This is different from graphite in which the volume change mainly occurs in the z direction. To further study the cycling stability, we calculate the stress–strain relationships of m-C_{16} within the range of 5% volume compressive strain and tensile strain. The corresponding results are presented in Fig. 5. The stress increases continuously with the rising strain and displays a nearly linear dependence within a large range of compressive and tensile strain, and no unexpected decrease or nonlinear platform cloud be found, which suggests that m-C_{16} can sustain a substantial volume change, indicating excellent cycling stability.

We also study the migration energy barrier of lithium ions under 5% compressive and tensile strains, and the detailed results are shown in Fig. 6. We can see that the compressive strain increases the energy barrier from 0.25 eV to 0.27 eV, while the tensile strain reduces the energy barrier from 0.25 eV to 0.10 eV. Getting a close look at the strained m-C_{16} structures, we find that tensile strains can increase the diffusion channel size and reduce the interaction between Li ions and the m-C_{16} host, while compressive strains have the opposite effect. Hence, the diffusion channel size has a great influence on the migration energy barrier. This is similar to the case of graphite where the interlayer distance has a decisive effect on the migration of in-plane Li ions.[61]

4. Conclusions

In summary, by employing the DFT method with the corrections of van der Waals interaction, we have investigated the probability of using carbon-based topological semimetal m-C_{16} as a LIB anode material. Based on systematic studies on the energetics and kinetic properties of Li-ion insertion and diffusion, we can draw the following main conclusions: (i) Li atoms donate almost all valence electrons to m-C_{16}, leading to a strong ionic binding with the substrate; (ii) the Li ions diffuse along the 1D channel in m-C_{16} with a quite small migration energy

barrier of 0.25 eV that is lower than the value of 0.53 eV in topological semimetal bco-C_{16}; (iii) the maximum capacity of m-C_{16} is 558 mA h g^{-1}, corresponding to Li–C_4, which is much higher than that of graphite (Li–C_6); (iv) the average voltage is 0.56 V, which can supply larger operating voltage and capacity once connected with the cathode; (v) the volume change during the Li insertion/de-insertion process is 3.6%, much smaller than that of topological semimetal bco-C_{16} (13.4%) reported recently;[37] and the 1D Li-ion diffusion properties are robust against compressive and tensile strains. Considering all these remarkable features of m-C_{16}, it would have great potential to be applied as an anode material for LIBs. We wish that the present study could promote further experimental effort on developing novel all-carbon-based topological LIBs anode materials with high capacity and fast kinetics.

Conflicts of interest

There are no conflicts to declare.

Acknowledgements

This work is partially supported by grants from the National Natural Science Foundation of China (21573008 and 21773003) and from the National Key Research and Development Program of China (2016YFB0100200). The calculations are supported by the High-performance Computing Platform of Peking University.

References

1 M. Armand and J. M. Tarascon, *Nature*, 2008, **451**, 652.
2 D. D. Sarma and A. K. Shukla, *ACS Energy Lett.*, 2018, **3**, 2841–2845.
3 N. Mahmood, C. Zhang, H. Yin and Y. Hou, *J. Mater. Chem. A*, 2014, **2**, 15–32.
4 G. Xu, B. Ding, J. Pan, P. Nie, L. Shen and X. Zhang, *J. Mater. Chem. A*, 2014, **2**, 12662–12676.
5 B. Dunn, H. Kamath and J.-M. Tarascon, *Science*, 2011, **334**, 928–935.
6 J. Liu, X. Li, Q. Wang, Y. Kawazoe and P. Jena, *J. Mater. Chem. A*, 2018, **6**, 13816–13824.
7 Y. Zhu, X. He and Y. Mo, *J. Mater. Chem. A*, 2016, **4**, 3253–3266.
8 S. Zhao, W. Kang and J. Xue, *J. Mater. Chem. A*, 2014, **2**, 19046–19052.
9 A. Urban, D.-H. Seo and G. Ceder, *npj Comput. Mater.*, 2016, **2**, 16002.
10 S. Shi, L. Xu, C. Ouyang, Z. Wang and L. Chen, *Ionics*, 2006, **12**, 343–347.
11 X. Zhang, Z. Zhang and Z. Zhou, *J. Energy Chem.*, 2018, **27**, 73–85.
12 S. Shi, C. Ouyang, M. Lei and W. Tang, *J. Power Sources*, 2007, **171**, 908–912.
13 C. Ouyang, Y. Du, S. Shi and M. Lei, *Phys. Lett. A*, 2009, **373**, 2796–2799.
14 J. B. Goodenough and Y. Kim, *Chem. Mater.*, 2010, **22**, 587–603.
15 M. Hu, X. Pang and Z. Zhou, *J. Power Sources*, 2013, **237**, 229–242.
16 Y. Nan, S. Li, B. Li and S. Yang, *Nanoscale*, 2019, **11**, 2194–2201.
17 Y. Wang, H. Li, P. He, E. Hosono and H. Zhou, *Nanoscale*, 2010, **2**, 1294–1305.
18 W. Sun and Y. Wang, *Nanoscale*, 2014, **6**, 11528–11552.
19 E. M. Erickson, C. Ghanty and D. Aurbach, *J. Phys. Chem. Lett.*, 2014, **5**, 3313–3324.
20 J. Sun, G. Zheng, H.-W. Lee, N. Liu, H. Wang, H. Yao, W. Yang and Y. Cui, *Nano Lett.*, 2014, **14**, 4573–4580.
21 H.-T. Kwon, C. K. Lee, K.-J. Jeon and C.-M. Park, *ACS Nano*, 2016, **10**, 5701–5709.
22 X. Wang, L. Qiao, X. Sun, X. Li, D. Hu, Q. Zhang and D. He, *J. Mater. Chem. A*, 2013, **1**, 4173–4176.
23 L. Su, Z. Zhou, X. Qin, Q. Tang, D. Wu and P. Shen, *Nano Energy*, 2013, **2**, 276–282.
24 L. Baggetto, E. Allcorn, R. R. Unocic, A. Manthiram and G. M. Veith, *J. Mater. Chem. A*, 2013, **1**, 11163–11169.
25 Y. Li, D. Wu, Z. Zhou, C. R. Cabrera and Z. Chen, *J. Phys. Chem. Lett.*, 2012, **3**, 2221–2227.
26 W.-H. Ryu, J. Shin, J.-W. Jung and I.-D. Kim, *J. Mater. Chem. A*, 2013, **1**, 3239–3243.
27 S. Abouali, M. Akbari Garakani, B. Zhang, H. Luo, Z.-L. Xu, J.-Q. Huang, J. Huang and J.-K. Kim, *J. Mater. Chem. A*, 2014, **2**, 16939–16944.
28 F. Yao, D. T. Pham and Y. H. Lee, *ChemSusChem*, 2015, **8**, 2284–2311.
29 J. Sun, H. Liu, X. Chen, D. G. Evans, W. Yang and X. Duan, *Adv. Mater.*, 2013, **25**, 1125–1130.
30 V. Etacheri, C. Wang, M. J. O'Connell, C. K. Chan and V. G. Pol, *J. Mater. Chem. A*, 2015, **3**, 9861–9868.
31 Y. Jing, Z. Zhou, C. R. Cabrera and Z. Chen, *J. Mater. Chem. A*, 2014, **2**, 12104–12122.
32 X. Zhang, Z. Ma, X. Zhao, Q. Tang and Z. Zhou, *J. Mater. Chem. A*, 2015, **3**, 4960–4966.
33 L. Ji, Z. Lin, M. Alcoutlabi and X. Zhang, *Energy Environ. Sci.*, 2011, **4**, 2682–2699.
34 X. Feng, Q. Wu, Y. Cheng, B. Wen, Q. Wang, Y. Kawazoe and P. Jena, *Carbon*, 2018, **127**, 527–532.
35 J.-T. Wang, H. Weng, S. Nie, Z. Fang, Y. Kawazoe and C. Chen, *Phys. Rev. Lett.*, 2016, **116**, 195501.
36 Y. Qie, J. Liu, S. Wang, Q. Sun and P. Jena, *J. Mater. Chem. A*, 2019, **7**, 5733–5739.
37 J. Liu, S. Wang and Q. Sun, *Proc. Natl. Acad. Sci. U. S. A.*, 2017, **114**, 651–656.
38 G. Ceder, Y. M. Chiang, D. R. Sadoway, M. K. Aydinol, Y. I. Jang and B. Huang, *Nature*, 1998, **392**, 694–696.
39 X. Zhang, Z. Zhang, S. Yao, A. Chen, X. Zhao and Z. Zhou, *npj Comput. Mater.*, 2018, **4**, 13.
40 S. Wang, Q. Bai, A. M. Nolan, Y. Liu, S. Gong, Q. Sun and Y. Mo, *Angew. Chem., Int. Ed.*, 2019, DOI: 10.1002/anie.201901938.
41 J. Liu, S. Wang and Q. Sun, *Proc. Natl. Acad. Sci. U. S. A.*, 2017, **114**, 651–656.

42 J. Liu, S. Wang, Y. Qie, C. Zhang and Q. Sun, *Phys. Rev. Mater.*, 2018, **2**, 025403.
43 S. Wang, J. Liu and Q. Sun, *J. Mater. Chem. A*, 2017, **5**, 16936–16943.
44 S. Shi, J. Gao, Y. Liu, Y. Zhao, Q. Wu, W. Ju, C. Ouyang and R. Xiao, *Chin. Phys. B*, 2016, **25**, 018212.
45 G. Kresse and J. Furthmüller, *Phys. Rev. B: Condens. Matter Mater. Phys.*, 1996, **54**, 11169.
46 G. Kresse and D. Joubert, *Phys. Rev. B: Condens. Matter Mater. Phys.*, 1999, **59**, 1758.
47 J. P. Perdew, K. Burke and M. Ernzerhof, *Phys. Rev. Lett.*, 1996, **77**, 3865.
48 S. Grimme, *J. Comput. Chem.*, 2006, **27**, 1787–1799.
49 G. Henkelman, B. P. Uberuaga and H. Jónsson, *J. Chem. Phys.*, 2000, **113**, 9901–9904.
50 G. Henkelman and H. Jónsson, *J. Chem. Phys.*, 2000, **113**, 9978–9985.
51 J. Liu, T. Zhao, S. Zhang and Q. Wang, *Nano Energy*, 2017, **38**, 263–270.
52 J. Liu, S. Wang, Y. Qie, J. Yu and Q. Sun, *Carbon*, 2018, **140**, 680–687.
53 K. Persson, V. A. Sethuraman, L. J. Hardwick, Y. Hinuma, Y. S. Meng, A. Van Der Ven, V. Srinivasan, R. Kostecki and G. Ceder, *J. Phys. Chem. Lett.*, 2010, **1**, 1176–1180.
54 C. Uthaisar and V. Barone, *Nano Lett.*, 2010, **10**, 2838–2842.
55 Q. Tang, Z. Zhou and P. Shen, *J. Am. Chem. Soc.*, 2012, **134**, 16909–16916.
56 D. Er, J. Li, M. Naguib, Y. Gogotsi and V. B. Shenoy, *ACS Appl. Mater. Interfaces*, 2014, **6**, 11173–11179.
57 D. Wu, Z. Xie, Z. Zhou, P. Shen and Z. Chen, *J. Mater. Chem. A*, 2015, **3**, 19137–19143.
58 Y. Jing, Z. Zhou, C. R. Cabrera and Z. Chen, *J. Phys. Chem. C*, 2013, **117**, 25409–25413.
59 D. Çakır, C. Sevik, O. Gülseren and F. M. Peeters, *J. Mater. Chem. A*, 2016, **4**, 6029–6035.
60 M. V. Koudriachova, N. M. Harrison and S. W. de Leeuw, *Solid State Ionics*, 2002, **152**, 189–194.
61 K. Persson, Y. Hinuma, Y. S. Meng, A. Van der Ven and G. Ceder, *Phys. Rev. B: Condens. Matter Mater. Phys.*, 2010, **82**, 125416.